

Pulse duration constraint of whistler waves in magnetized dense plasma

Masayasu Hata,^{1,2,*} Takayoshi Sano¹, Yasuhiko Sentoku¹, and Hideo Nagatomo¹

¹*Institute of Laser Engineering, Osaka University, Suita, Osaka 565-0871, Japan*

²*Kansai Photon Science Institute (KPSI), National Institutes for Quantum and Radiological Science and Technology (QST), Kizugawa, Kyoto 619-0215, Japan*

Hitoshi Sakagami¹

National Institute for Fusion Science, National Institutes of Natural Sciences, Toki, Gifu 509-5292, Japan

 (Received 3 March 2021; revised 16 June 2021; accepted 31 August 2021; published 17 September 2021)

Interactions between large-amplitude laser light and strongly magnetized dense plasma have been investigated by one- and two-dimensional electromagnetic particle-in-cell simulations. Since whistler waves have no critical density, they can propagate through plasmas beyond the critical density in principle. However, we have found that the propagation of whistler waves is restricted significantly by the stimulated Brillouin scattering. It is confirmed that the period during which the whistler wave can propagate in overcritical plasmas is proportional to the growth time of the ion-acoustic wave via the Brillouin instability. The allowable pulse duration of the whistler wave has a power-law dependence on the amplitude of the whistler wave and the external magnetic field.

DOI: [10.1103/PhysRevE.104.035205](https://doi.org/10.1103/PhysRevE.104.035205)

I. INTRODUCTION

The establishment of a method for generating kilotesla (kT) order magnetic fields using high-power laser allows us to examine experimentally laser-plasma interactions (LPIs) under strong external magnetic fields [1–4]. Such a strong magnetic field affects not only the dynamics of fast electrons induced in LPIs but also the laser propagation itself. For example, the magnetized fast ignition scheme has been proposed as a new design of inertial confinement fusion, in which fast electrons guided by a kT-order magnetic field are expected to heat an imploded dense core isochorically [5–7].

When a strong magnetic field, of which the cyclotron frequency exceeds an electromagnetic wave frequency ω , is applied along the wave propagation direction, the critical density of the right-handed circularly polarized (RCP) wave disappears [8]. The critical strength of the magnetic field is thus defined as $B_{\text{cr}} \equiv m_e \omega / e$, where m_e and e are the electron mass and the charge, respectively. The wave with this cutoff-free phenomenon, the so-called “whistler wave,” is well known in the geosciences, space sciences, and magnetic confinement fusion. However, the whistler wave propagation had not been clarified, especially for the cases with high frequencies and large amplitudes like ultrahigh intense laser lights. This is due to the technological difficulty of inducing the kT-order magnetic field required for the high-frequency whistler wave propagation. Recent breakthroughs in generating strong magnetic fields driven by intense laser lights with capacitor coils provide access to a new parameter regime of large-amplitude whistler waves in dense plasmas.

In order to generate a large-amplitude whistler wave experimentally, it requires both high-intensity electromagnetic waves (laser lights) and strong magnetic fields over the critical

strength B_{cr} . Notice that the longer wavelength can reduce the critical strength significantly. Owing to the chirped pulse amplification (CPA) [9], the laser intensity becomes strong enough to accelerate electrons up to relativistic velocity with the laser wavelength of around $1 \mu\text{m}$ [10–13]. The CPA technique is applicable to a light with longer wavelength such as CO_2 lasers to achieve the relativistic intensity [14]. For a CO_2 laser with a wavelength of $10 \mu\text{m}$, the critical field strength for whistler wave propagation is about 1 kT, which is about the same as the current achievement in laser experiments. Therefore, it will be feasible to study the physics of large-amplitude whistler waves by using CO_2 lasers in the near future. In space plasmas, the required magnetic field becomes much weaker. For example, it corresponds to 100 (1) μT for 3 MHz (30 kHz) radio waves in the Earth’s ionosphere, and 100 nT for 3 kHz radio waves in the magnetosphere [15–18].

The application of external magnetic fields to the ultraintense laser-plasma interaction brings various interesting phenomena. For example, when the magnetic field is below the critical magnetic field B_{cr} , a magnetic vortex is generated in a weakly magnetized beam plasma system [19,20]. A moderate magnetic field below B_{cr} can guide fast electron beams efficiently [5], which has been observed via the measurement of coherent transition radiation of fast electrons [21]. Electron cyclotron resonance due to a circularly polarized (CP) laser will occur at $B = B_{\text{cr}}$, and the resonance condition in terms of the magnetic field strength broadens due to the relativistic effects [22]. When the magnetic field is over B_{cr} , the R wave, the CP wave rotating clockwise along the direction of the magnetic field, can propagate into dense plasma without cutoff. In contrast, the L wave rotating counterclockwise propagates only up to the L-cutoff density. Such wave propagation characteristics in the nonrelativistic regime were demonstrated by Luan *et al.* [23]. In the relativistic regime, Yang *et al.* [24] reported that the relativistic R-wave pulse heats the electrons trapped in the wakefield excited in the magnetized dense

*hata.masayasu@qst.go.jp

plasma. Recently, the idea of ultrafast ion heating by colliding whistler waves was proposed by Sano *et al.* [25]. The colliding two whistler waves form standing waves where the electromagnetic waves transfer energy directly to ions, which is far more efficient than the conventional methods such as fast electron heating and shock wave heating [26].

In this paper, we focus on the allowable pulse duration of the whistler waves. Interestingly, whistler waves are intermittently observed in the solar wind, but the origin of the intermittency is still unclear [27,28]. Therefore, it would be essential to investigate the time window during which the whistler waves can propagate in dense plasmas. From the early 1970s, parametric decay instabilities of electromagnetic waves propagating along an external magnetic field had been studied intensely [29–32]. We pay attention again to such instabilities because they might disturb the plasma and thus determine the time window of the whistler wave propagation. Compared to the previous studies, we consider electromagnetic waves with much larger amplitude, namely, relativistic laser lights.

In this paper, we evaluate numerically the transmittable pulse duration of laser-generated whistler waves with the help of one- (1D) and two-dimensional (2D) relativistic electromagnetic particle-in-cell codes, PICLS [33]. The outline of this paper is as follows. In Sec. II we demonstrate the interaction of a linearly polarized laser light and an overcritical plasma with a strong external magnetic field over the critical magnetic field using the 2D code. The penetration feature of the incident light beyond the critical density is observed. Here the differences of the propagation characteristics between the RCP and the left-handed circularly polarized (LCP) waves are discussed.

Next, we concentrate our discussion on the whistler wave and estimate the scaling of its transmittable duration as a function of the normalized wave amplitude and the applied magnetic field strength, conducting a series of 1D simulations with various parameter sets. In Sec. III we have performed the attentive measurement of the whistler wave propagation and found that the inverse of the growth rate of the ion-acoustic wave due to the stimulated Brillouin scattering (SBS) determines the time window of a transmittable whistler wave. Section IV is dedicated to the summary.

II. SIMULATIONS

A. 2D demonstration

The cutoff of electromagnetic waves traveling along magnetic fields disappears when the magnetic field strength exceeds the critical value. Then the electromagnetic waves can propagate in plasmas with overcritical densities as the whistler wave. Here the propagation characteristic of the whistler waves is investigated using the 2D PICLS code to reveal the interaction between a linearly polarized laser light and an overcritical plasma with an application of a strong external magnetic field.

1. Simulation setup

The target plasma in our simulation is made of fully ionized carbon and hydrogen ions in equal proportion. The initial density profile of the plasma consists of three parts. The primary

plasma has a flat electron density profile with a density of $20n_{cr}$ and a length of $85\lambda_L$. Here λ_L is the laser wavelength and $n_{cr} = \epsilon_0 m_e \omega_L^2 / e^2$ is the critical density, where ϵ_0 and ω_L are the vacuum permittivity and the angular frequency of laser light, respectively. The front rarefied plasma has an exponential electron density profile with a scale length of $20\lambda_L$ from $0.1n_{cr}$ up to $20n_{cr}$. At the rear of the primary plasma, there is tenuous plasma having an exponential electron density profile with a scale length of $8\lambda_L$ from $20n_{cr}$ to $0.1n_{cr}$ to reduce the light reflection at the sharp plasma edge. Figure 1(a) shows the spatial profile of the initial electron density of the front part of the plasma. The density profile in the y direction is uniform. Note here that the simulation scale and the plasma density could scale up or down by the laser wavelength since it is a purely kinetic simulation. The applied external magnetic field B_{ext} along the direction of laser propagation (x axis) is set to $5B_{cr}$, which corresponds to 5 or 50 kT for the laser wavelength of 10 or 1 μm , for example. A linearly polarized laser with temporal flattop and spatial Gaussian profiles irradiates from the left boundary ($x = 0$). The spot diameter is assumed to be $20\lambda_L$. The normalized amplitude of the laser electric field $a_0 \equiv eE_L / (m_e \omega_L c)$ is 1.0, which corresponds to 1.37×10^{16} or 1.37×10^{18} W/cm² for the 10 or 1 μm laser wavelength. Here E_L and c are the electric field of laser light and the speed of light. We adopt the absorbing boundary condition for electromagnetic fields and the reflection boundary condition for particles except fast electrons with the Lorentz factor more than 2. These fast electrons are absorbed at x -boundaries, although not many electrons could reach the x -boundaries during the whole simulation time of $195\tau_L$, where τ_L is the laser period. The time and spatial resolutions are 40 time steps per laser period and 40 cells per laser wavelength, and the particle numbers per cell are 11, 1, and 5 for electrons, C, and H ions, respectively. The fourth-order spline interpolation is taken into account to suppress numerical heating.

2. Results of 2D PIC simulations

Figure 1 shows the initial electron density profile and temporal evolutions of the electromagnetic field amplitude $\sqrt{(eE/m_e \omega_L c)^2 + (eB/m_e \omega_L)^2}$ in the plasma, where the electromagnetic field does not include the external magnetic field. (Hereafter the external magnetic field is excluded for whole observation.) A linearly polarized light can be considered as superposition of RCP and LCP waves to the direction of the light propagation. In the presence of the strong magnetic field along with the propagation path, the linearly polarized light separates into the R and L waves naturally. It is noted that the polarity of CP waves is defined by the direction of the wave-number vector, while the R or L wave rotation is defined by the direction of the magnetic field. For all simulations conducted in this paper, the direction of the external magnetic field is the same as that of the incident laser wave-number vector so that the R and L waves correspond to the RCP and LCP waves, respectively. According to the linear dispersion relation, there is the cutoff at the density $n_L/n_{cr} = 1 + B_{ext}/B_{cr}$ for the L wave. In the current simulation with $B_{ext} = 5B_{cr}$, the L cutoff is six times the critical density at $x = 91\lambda_L$. On the other hand, the whistler mode of the R wave has no cutoff. Figure 1(b) shows that both the R and L waves propagate in the dense region beyond n_{cr} . The incident laser propagates as

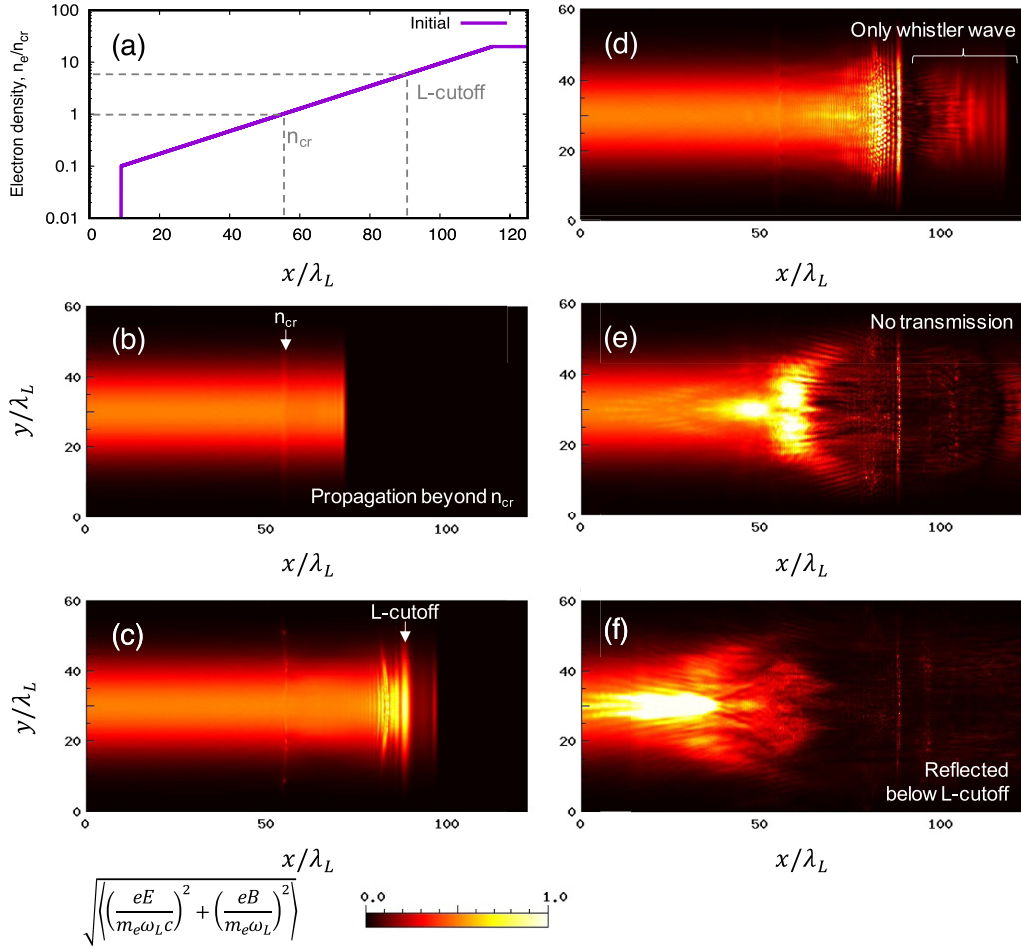


FIG. 1. (a) Initial electron density and the electromagnetic field amplitude at $t =$ (b) $75\tau_L$, (c) $105\tau_L$, (d) $135\tau_L$, (e) $165\tau_L$, and (f) $195\tau_L$ at the front of the target. Both R and L waves can propagate till the L cutoff of $6n_{cr}$ and the L wave is reflected at the L cutoff. An R wave having no cutoff can initially propagate into dense plasma more than $6n_{cr}$, but it finally cannot propagate.

the linearly polarized form till the position of $x = 91\lambda_L$ where the electron density is $n_e = 6n_{cr}$. At $t = 105\tau_L$ [Fig. 1(c)], the laser light reaches the L cutoff, then the L-wave component is reflected, and only the R-wave component propagates further into the denser region at $x > 91\lambda_L$. At $t = 135\tau_L$ [Fig. 1(d)], the electromagnetic wave observed in the region $x > 91\lambda_L$ is only the whistler wave. Additionally, the standing wave due to the incident and reflected L waves can be seen at $60\lambda_L < x < 90\lambda_L$. It is known that the standing CP wave causes efficient plasma heating and its collapse excites the large density modulations [25]. Actually, ions in the region are heated up to 20 keV on average. Then the large density modulations are caused by the collapse of the standing L wave, and the injected electromagnetic wave is reflected below the L cutoff as shown in Fig. 1(f). At $t = 165\tau_L$ and later [Figs. 1(e) and 1(f)], the amplitude of the whistler wave decreases, and finally no whistler waves are seen in the dense plasma of $n_e > 6n_{cr}$ despite that the laser light keeps irradiating with constant intensity. This 2D simulation demonstrates that there is a time window in which the whistler wave can go forward in the overcritical plasmas.

The above phenomena can be realized in 1D simulations as well with the same initial parameters. Figure 2 shows the comparison of the electromagnetic field amplitudes in

1D and 2D simulations at $t = 135\tau_L$, where the green line represents the electromagnetic field in the 1D simulation and the sky-blue line is a cross section in the 2D simulation at the center ($y = 30\lambda_L$). The dashed line indicates the position at the L cutoff. The behaviors of the electromagnetic wave are almost identical in both 1D and 2D simulations. Therefore, for simplicity, 1D simulations are adopted in the following analysis. Hereafter, we focus only on the propagation features of the R waves in overcritical plasma or the whistler waves.

B. 1D analysis

The 2D simulation shows that the duration of the whistler wave has a finite limit. To investigate this feature quantitatively, we perform a series of 1D simulations of R-wave propagation in magnetized dense plasmas. Here the key parameters are the laser amplitude and the external magnetic field.

1. Simulation setup

A hydrogen target having a flat density profile with a thickness of $50\lambda_L$ and a density of $60n_{cr}$ is set in 1D geometry. Plasmas with exponential density profiles are placed in front of and behind the flat-density target with a scale length of

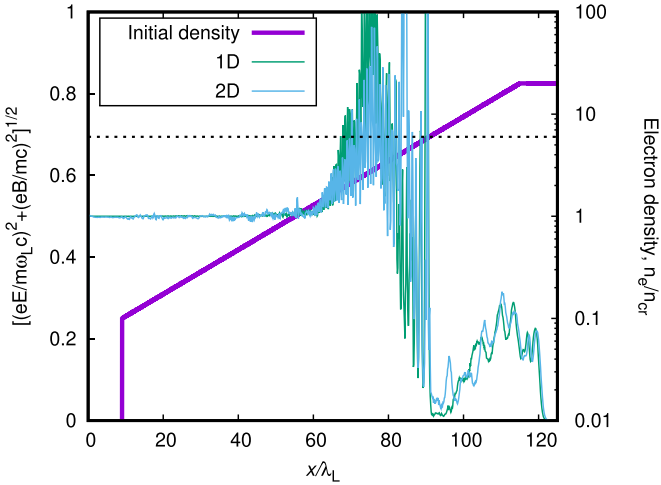


FIG. 2. Comparison of the electromagnetic field amplitudes between one- and two-dimensional simulations at $t = 135\tau_L$, where purple, green, and sky-blue lines represent initial electron density, 1D electromagnetic field, and cross section of the 2D electromagnetic field at the center ($y = 30\lambda_L$), respectively, and the dashed line indicates the L cutoff of six times the critical density. Initial parameters are the same on both 1D and 2D simulations except the laser spatial profile.

L_{sc} from $0.1n_{cr}$ to $60n_{cr}$. To clarify the effects of the scale length, a wide range of L_{sc} is considered from 1 to $20\lambda_L$. As a fiducial model, the scale length is set to $1\lambda_L$. The initial electron density profile of the fiducial model is shown in Figs. 3(a) and 3(b) with a black-dashed line. An RCP laser light, which penetrates into the magnetized plasma as the whistler wave, comes from the left boundary, and its temporal profile is semi-infinite. A uniform external magnetic field is applied along the direction of the laser propagation with the strength of $B_{ext} = 5B_{cr}$ in the same way as the 2D simulation. We use the absorbing boundaries for the electromagnetic fields and the reflection ones for particles. In order to remove the boundary effects, sufficiently large vacuum regions are prepared at both the front and rear of the plasma. The size of the computational domain is thus set to $350\lambda_L$, and the flat plasma is placed at $150 \leq x \leq 200\lambda_L$. The normalized laser amplitude considered here is ranging from $a_0 = 0.01$ to the relativistic amplitude $a_0 = 1$. The PICLS1D simulations have been carried out until $t = 3000\tau_L$ for the $a_0 = 0.01$ cases and $750\tau_L$ for the other cases. The number of electrons (ions) per cell is 50 (50), and the temporal and spatial resolutions are set to 100 time steps per laser period and 100 cells per laser wavelength, where the cyclotron motion in the strong magnetic field of $B_{ext} = 5B_{cr}$ is well resolved.

2. Results of 1D PIC simulations

The 1D PIC simulations reproduce the temporal constraint of whistler waves as seen in 2D PIC simulations. We found that the constraint strongly depends on the wave amplitude as shown in Fig. 3. Each figure shows the time evolutions of electric fields perpendicular to the external magnetic field for the cases of (a) $a_0 = 0.01$ and (b) 1.0 and snapshots of y and z components of the transverse electric field for (c) $a_0 = 0.01$ at $t = 360\tau_L$ and (d) $a_0 = 1.0$ at $t = 240\tau_L$.

The laser-generated whistler wave shows the stable propagation in the dense target for a relatively longer time in the case of the weak amplitude $a_0 = 0.01$. The amplitudes of the transverse electric field are unchanged before and after the propagation in the dense plasma region, showing almost perfect transparency of the RCP wave. Under the condition of the perfect transparency, the normalized amplitude of the laser-generated whistler wave in the plasma is expressed as

$$a_W \equiv \frac{eE_W}{m_e\omega_L c} = \frac{1}{\sqrt{N}} \frac{eE_L}{m_e\omega_L c} = \frac{a_0}{\sqrt{N}}, \quad (1)$$

with the refractive index N , given as

$$N = \left(1 - \frac{\omega_{pe}^2/\omega_L^2}{1 - \omega_{ce}/\omega_L}\right)^{1/2} \quad (2)$$

where ω_{ce} indicates the electron cyclotron frequency. The refractive index is $N = 4$ in the current setup, and the observed amplitude agrees well with the half of the incident one. Later at $t = 720\tau_L$, the whistler wave starts to be reflected partially at the front plasma. Finally (at $t = 1500\tau_L$), the wave is totally reflected so that no transmission to the rear vacuum is observed.

In contrast, when $a_0 = 1.0$, the reflection occurs much earlier, so that only a short pulse about $10\lambda_L$ of the laser-generated whistler wave can propagate into the dense plasma, as seen in Figs. 3(b) and 3(d). The transmitted whistler wave recovers its amplitude with slight modulations. Thus, the transmittable pulse duration obviously depends on the laser amplitude.

The dependence of the transmitted pulse duration of the laser-generated whistler wave is studied on the normalized laser amplitude a_0 , the scale length L_{sc} of the front plasma, and the external magnetic field B_{ext} . The transmitted pulse duration is evaluated as the full width at the half maximum of the amplitude in the vacuum region behind the plasma. We perform 18 runs with different combinations of the parameters and summarize the results in Fig. 4. Despite the difference in the magnetic field strength and the scale length, the tendency of the transmitted pulse duration to a_0 shows a similar dependence with the same power law. The averaged power index of all the six parameter sets is -0.66 ± 0.08 , which is shown by the dashed line in Fig. 4. The transmitted pulse duration is longer for the cases of the stronger magnetic field or the longer scale length. For all cases, the laser-generated whistler waves are eventually reflected so that the transmittable pulse duration is limited to the finite duration.

For the cases of a scale length of $1\lambda_L$, precise simulations with higher resolution have been carried out to investigate the dependence of the transmitted pulse duration on the external magnetic field. The resolutions are set to 1000 time steps per laser period and 1000 cells per laser wavelength to capture the cyclotron motion in the strong magnetic field of $B_{ext} = 80B_{cr}$ at the maximum. Figure 5(a) shows the behaviors of transmitted pulse duration against the normalized laser amplitude for the cases of $B_{ext} = 5B_{cr}, 10B_{cr}, 20B_{cr}, 40B_{cr},$ and $80B_{cr}$. The dependence of the normalized laser amplitude shows the same scaling as in Fig. 4 except two cases of $(a_0, B_{ext}) = (2.0, 5B_{cr})$ and $(5.0, 10B_{cr})$. In these two exceptional runs, the transmitted pulse may be too short to evaluate the duration

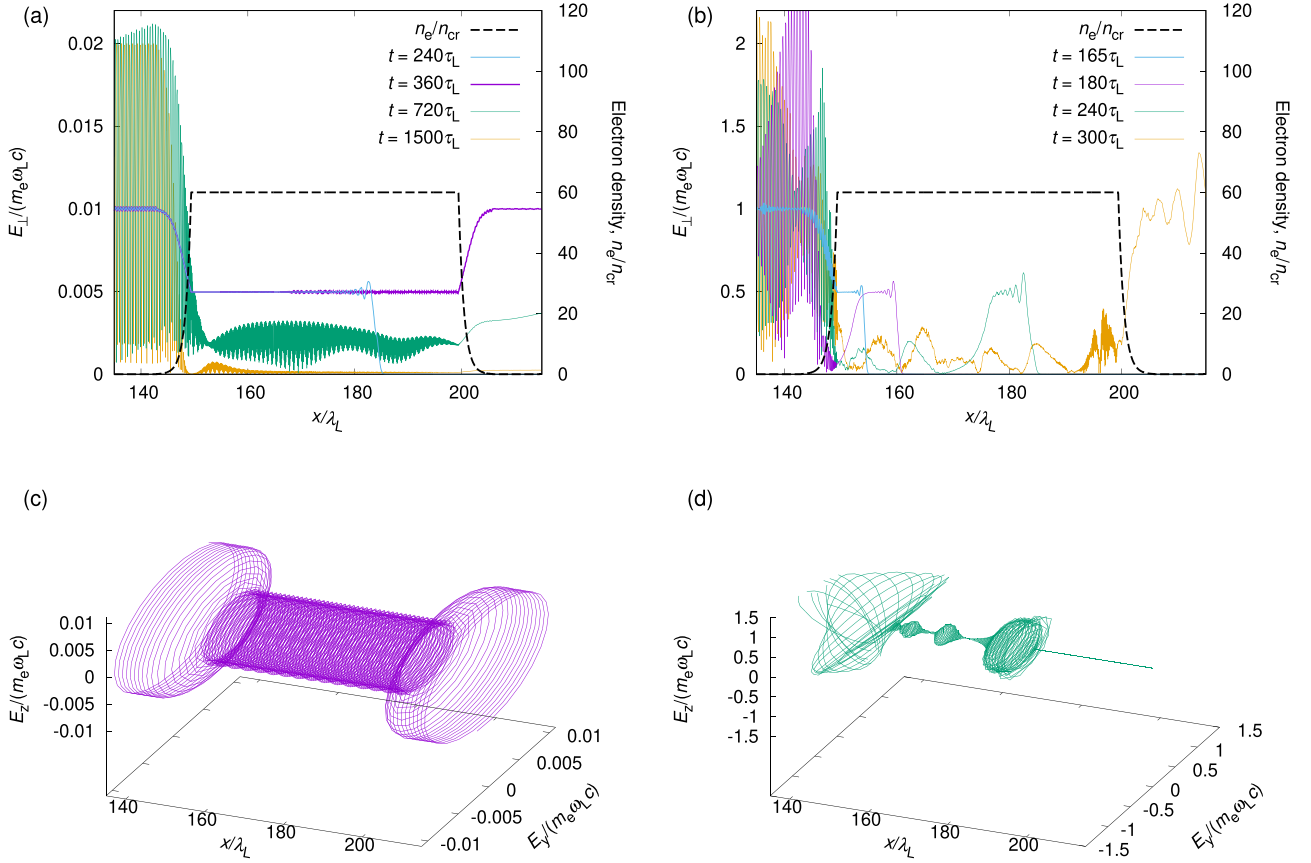


FIG. 3. Upper panels show the time evolution of perpendicular electric fields of electromagnetic wave in the cases of (a) $a_0 = 0.01$ and (b) 1.0, where each color indicates the electric fields at the corresponding time and the black dashed line indicates the initial electron density. Lower panels show snapshots of the y and z components of the perpendicular electric field at (c) $a_0 = 0.01$, $t = 360\tau_L$ and (d) $a_0 = 1.0$, $t = 240\tau_L$.

correctly. Thus, hereafter, these two cases are ignored in the fitting analysis.

The transmittable whistler wave depends clearly on the laser amplitude and the external magnetic field, whereas the plasma scale length has little influence. In magnetized dense

plasmas, the normalized amplitude of whistler waves is different from that of the incident RCP laser in the vacuum. The propagation feature of the whistler waves should be determined by the whistler wave amplitude in the magnetized plasmas rather than the laser amplitude in the vacuum. According to our simulation results, the laser wave seems to transmit into magnetized dense plasmas almost entirely owing to the smooth density distribution of the plasma. Then the normalized amplitude of the laser-generated whistler wave is given by Eq. (1). Here we consider a fitting formula of the pulse duration τ as a power-law function of a_W and B_{ext} . Assuming the dependence as $\tau \propto a_W^{p_1} B_{\text{ext}}^{p_2}$, the simulation data for the cases of $a_0 = 0.1, 0.2, 0.5$, and 1.0 are fitted by the least-squares method. The obtained power indexes are $p_1 = -0.67$ and $p_2 = 0.86$, respectively. Since $p_1 \approx -p_2$, then almost all the simulation data are unified as a function of $a_W/(B_{\text{ext}}/B_{\text{cr}})$, which is shown by Fig. 5(b). The interpretation of this power-law dependence is discussed in the following section.

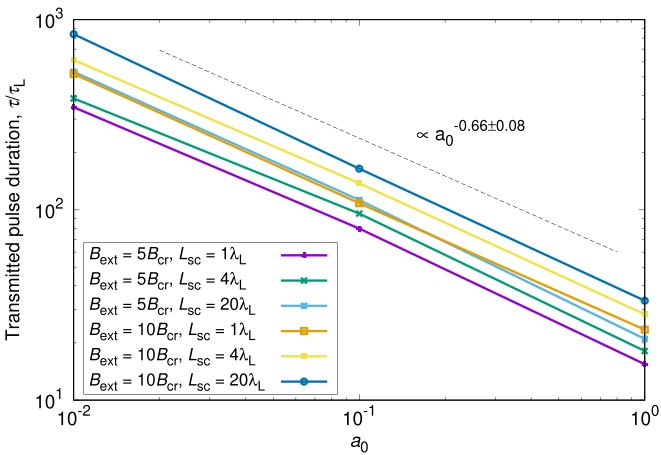


FIG. 4. Behavior of transmitted pulse duration against the normalized laser amplitude. All lines show the same tendency of a power law. The average power index of all the six color lines is -0.66 , which is plotted as a dashed line.

III. DISCUSSION

Numerical simulations reveal that there exists a constraint on the pulse duration of whistler waves. The SBS is one of the plausible mechanisms of this limitation. If the SBS is the cause, the pulse duration would be inversely proportional to the SBS growth rate. Here we perform additional simulations

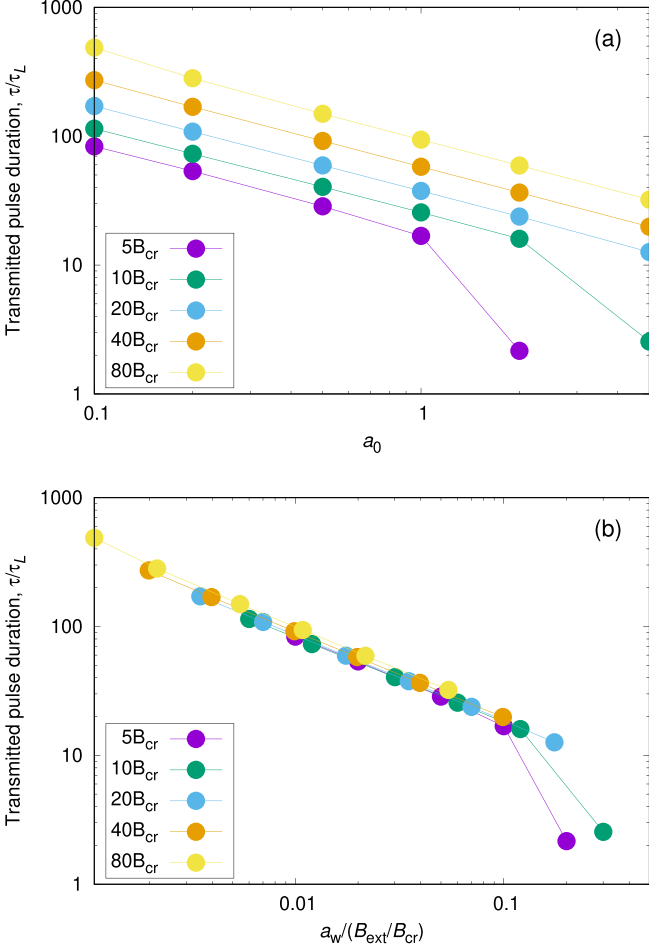


FIG. 5. Behaviors of transmitted pulse duration against (a) the normalized laser amplitude a_0 and (b) the production of the normalized amplitude of the whistler wave and the inverse of the external magnetic field $a_w/(B_{\text{ext}}/B_{\text{cr}})$.

to measure the growth rate of ion-acoustic waves due to the SBS. For the sake of simplicity, a uniform plasma with a thickness of $300\lambda_L$ is adopted as a target because the impact of the front exponential plasma can be ignored (see Fig. 4).

Figure 6 shows time evolutions of the perpendicular electric fields of an electromagnetic wave and ion phase space for the cases of $a_0 = 0.1$. The injected RCP wave starts to interact with the target at $t = 50\tau_L$ in this simulation. At $t = 360\tau_L$, the perpendicular electric field E_{\perp} is spatially constant inside the plasma. However, fluctuations in the perpendicular electric field increase gradually with time. Eventually, the injected RCP wave cannot propagate into the target and is reflected at the front surface at $t = 540\tau_L$. The generation of strong ion-acoustic waves is observed at the corresponding timing, as shown in Fig. 6(b). Simultaneously, the plasma density fluctuation occurs, and the average electron energy reaches to around 50 eV at the area where the laser cannot propagate. For comparison, a similar simulation with no external magnetic field has been conducted. We have checked that the injected RCP wave is completely reflected at the sharp interface, and no SBS is caused in the target plasma because the RCP wave cannot propagate into the overdense plasma.

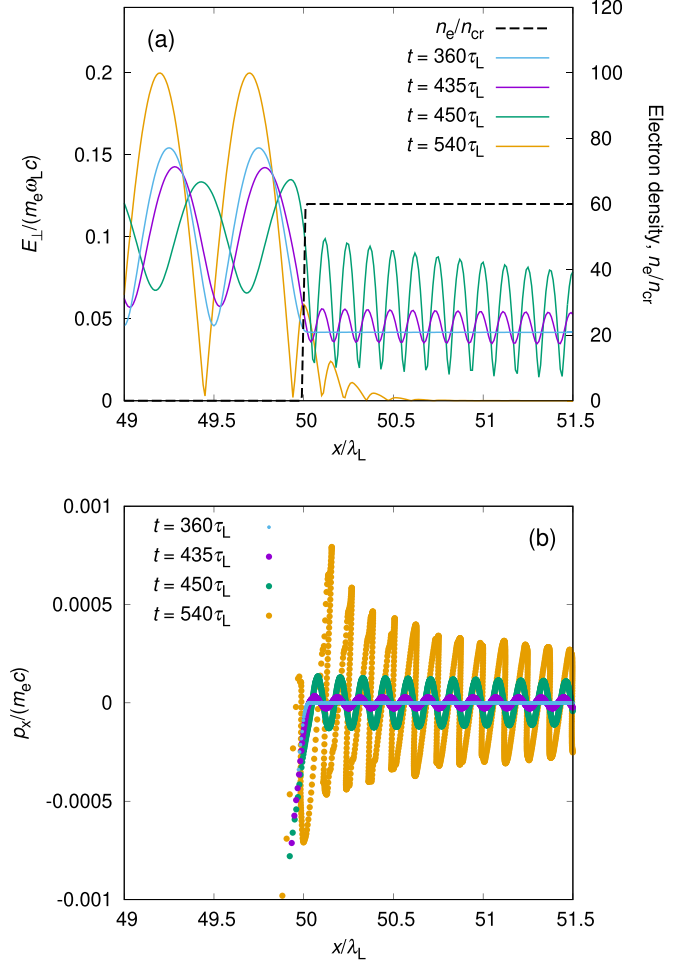


FIG. 6. Time evolutions of perpendicular electric fields of transverse electromagnetic wave (a) and ion phase space (b) in the cases of $a_0 = 0.1$, where each color indicates the corresponding time and the black dashed line indicates initial electron density.

The ion-acoustic wave amplitude is evaluated by phase-space snapshots at every laser cycle by fitting with a sinusoidal curve. Then the linear growth rate can be calculated from the time evolution of the amplitude. Figure 7 shows the obtained growth rate of ion-acoustic waves against the normalized laser amplitude a_0 . Eight runs for the cases of $a_0 = 0.025, 0.05, 0.1, 0.2, 0.4, 0.8, 1.6,$ and 3.2 have been conducted, where the other parameters are identical. The behavior of the growth rate exhibits a power-law dependence, although it is saturated for the relativistic intensity because it becomes comparable to the laser frequency. The best fit in the range from $a_0 = 0.025$ to $a_0 = 1.6$ is $0.34a_0^{0.67}$. Therefore, the transmitted pulse duration scales as $\tau \propto a_0^{-0.67}$, which agrees well with the numerical result shown in Fig. 4.

Furthermore, the comparison of the growth rates between the simulations and the theory reveals that the excitation of the ion acoustic wave is caused by the SBS. The linear growth rate of the ion acoustic wave due to the SBS in the cold limit has been derived as [29,30]

$$\frac{\gamma}{f_L} = \sqrt{3\pi}(2\alpha)^{1/3}, \quad (3)$$

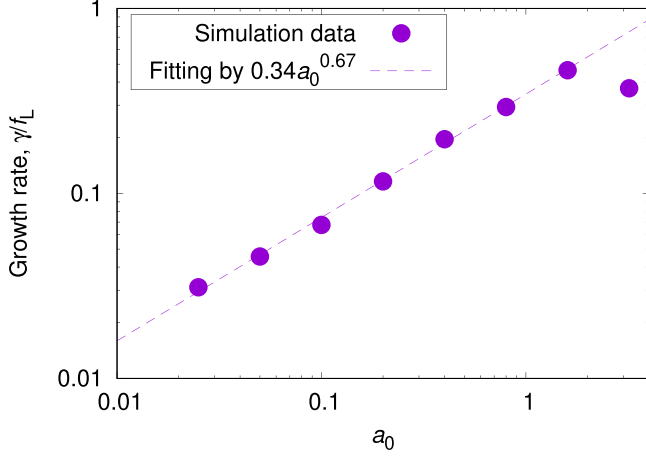


FIG. 7. The growth rate of an ion-acoustic wave estimated from 1D PIC simulations. The obtained data are fitted well by a function of $0.34a_0^{0.67}$. For the relativistic-intensity case of $a_0 > 1$, the growth rate seems saturated because it becomes comparable to the laser frequency.

where

$$\alpha = \frac{m_e}{m_i} \frac{B_{\text{cr}}}{B_{\text{ext}}} N^2 a_W^2. \quad (4)$$

Here f_L and m_i indicate the laser frequency and the ion mass, respectively. The normalized amplitude of a_W is expressed by $2a_0/(N+1)$ because of the transmission of the electromagnetic wave at uniform planar interface. Apparently, the growth rate increases with the amplitude of the whistler wave. It also has the dependence to the external magnetic field and the electron density, like $\propto B_{\text{ext}}^{-2}, n_e$ approximately. Then the analytical growth rate is estimated as $\gamma = 0.553a_0^{2/3}$ using the simulation condition, which is in good agreement with the formula of the observed growth rate.

The excitation of the ion-acoustic wave by the SBS causes significant density modulations in ion and electron density profiles. These density modulations induce the reflection of the electromagnetic wave (see the Appendix). The density-modulation structure is preserved until the end of the simulation after it is generated. Therefore, the reflection of the RCP wave continues throughout the calculation.

The transmittable pulse duration will be proportional to the inverse of the growth rate as $\tau/\tau_L = Af_L/\gamma$, where A is a proportional constant. Using the simulation results in Fig. 5, the correlation of the transmitted pulse duration against the theoretical growth rate is shown in Fig. 8. The proportional constant has weak dependence of the external magnetic field. For the cases of $5B_{\text{cr}}$ and $80B_{\text{cr}}$, the fitted values of A are 5.90 ± 0.05 and 13.2 ± 0.2 , respectively. Based on the all data in Fig. 8, the proportional constant is estimated as $A = 10.2 \pm 0.6$. Then we obtain a formula of the transmittable pulse duration as follows:

$$\frac{\tau}{\tau_L} = \frac{A}{\sqrt{3}\pi} \left(2 \frac{m_e}{m_i} \frac{B_{\text{cr}}}{B_{\text{ext}}} N^2 a_W^2 \right)^{-1/3}. \quad (5)$$

The transmittable pulse duration certainly scales as $\propto a_W^{-2/3}$. Furthermore, in the limit of $\omega_{\text{pe}}/\omega_L \gg B_{\text{ext}}/B_{\text{cr}} \gg 1$, the refractive index is approximately given by $N^2 \approx$

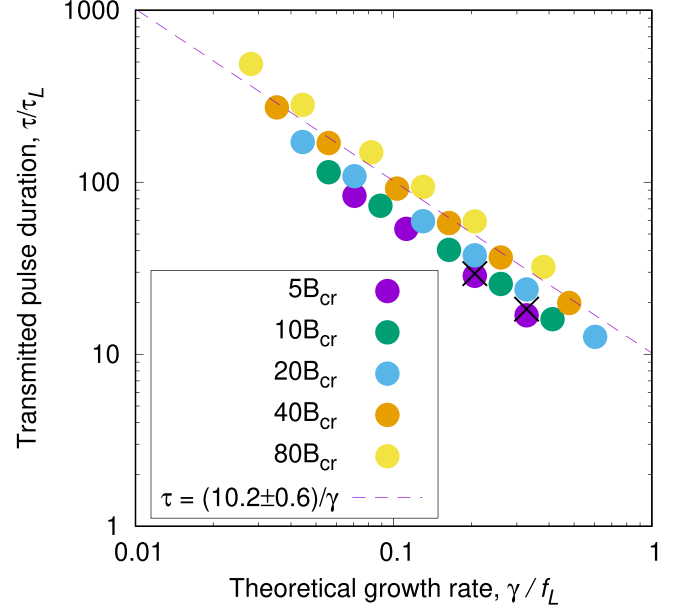


FIG. 8. The behavior of the transmitted pulse duration against the theoretical growth rate. The transmitted pulse duration τ/τ_L is proportional to the inverse of the growth rate f_L/γ . The proportional constant is estimated as around 10 by the fitting (dashed line). Two cross marks are obtained from 2D simulations of spatially uniform irradiation with the same setup of 1D simulations for the cases of $B_{\text{ext}} = 5B_{\text{cr}}$ and $a_0 = 0.5, 1.0$. The comparison between 1D and 2D simulations shows almost the same results.

$(\omega_{\text{pe}}^2/\omega_L^2)/(B_{\text{ext}}/B_{\text{cr}})$, and then the duration is given by

$$\frac{\tau}{\tau_L} \sim \frac{A}{\sqrt{3}\pi} \left(2 \frac{m_e}{m_i} \frac{\omega_{\text{pe}}^2}{\omega_L^2} \right)^{-1/3} \left(a_W \frac{B_{\text{cr}}}{B_{\text{ext}}} \right)^{-2/3}. \quad (6)$$

The transmittable pulse duration scales as $\propto (a_W/B_{\text{ext}})^{-2/3}$, which agrees well with the numerical results shown in Fig. 5(b). To lengthen the transmittable pulse, the normalized whistler-wave amplitude a_W should be smaller, and the external magnetic field should be stronger.

For comparison, 2D simulations of spatially uniform irradiation with the same setup of 1D simulations for the cases of $B_{\text{ext}} = 5B_{\text{cr}}$ and $a_0 = 0.5, 1.0$ have been conducted. The obtained transmitted pulse lengths are plotted as two cross marks in Fig. 8. It is confirmed that transmitted pulse lengths of 1D and 2D simulations are almost the same.

It will be useful to comment on the plasma heating using laser-generated whistler waves. According to the previous studies on the whistler-wave applications, electron cyclotron resonance heating [22] and ion heating via standing whistler waves [25,26] are expected as efficient heating methods. However, these applications would be inefficient if the whistler wave is terminated by the SBS. Therefore the transmitted pulse duration is the crucial parameter. In general, a plasma target irradiated by an intense laser is preexpanded due to the prepulse that is delivered before the main pulse. Thus, the main pulse must propagate in the preexpanded plasma with a smooth density distribution. In such a situation, the normalized amplitude of the laser-generated whistler wave a_W is expressed by that of the injected laser a_0 through Eq. (1).

Substituting Eq. (1) into Eq. (5), we can derive the formula of the transmittable pulse duration of a laser-generated whistler wave as a function of a_0 . The expression using the normalized laser amplitude is practical for the estimation of the transmittable pulse duration in actual laser experiments. According to this formula and our simulation study, it is found that whistler waves with a duration of a few tens of periods can propagate into a dense plasma of $n_e/n_{cr} = 60$ for the relativistic laser of $a_0 \sim 1$ with the external magnetic field of $B_{ext}/B_{cr} = 5$. Thus the direct interaction of a relativistic laser-generated whistler wave and dense plasma is achievable, and therefore the experiments for the demonstration of the plasma heating by the whistler waves could be realized.

IV. SUMMARY

The growth of the SBS constrains the transmittable pulse duration of whistler waves. In the simulations, the laser-generated whistler wave transmits the overcritical dense plasma at the early stage. However, it is gradually reflected due to the growth of ion-acoustic waves. As the result, the transmitted pulse duration is inversely proportional to the growth rate of ion-acoustic waves by the SBS. The whistler wave’s duration is proportional to the square of the third of the whistler wave amplitude and the inverse of the external magnetic field strength, i.e., $\tau \propto (a_W/B_{ext})^{2/3}$.

Our results ensure that whistler waves can propagate sufficiently longer term to realize novel heating scenarios due to whistler wave application in the dense plasmas, e.g., electron cyclotron resonance heating and ion heating via standing whistler waves [22,25,26]. For the case of the dense plasmas, such as a solid density plasma or imploded overcritical plasma, collisional effects also terminate the whistler wave. One example of the whistler wave application for thermonuclear fusion was reported and the collisional effects on whistler wave propagation in dense plasma were discussed [26]. For the application of the above heating mechanism using whistler waves for the laser fusion scheme, the effects of the SBS and collision should be considered to optimize the target design.

ACKNOWLEDGMENTS

We thank T. Johzaki and K. Mima for fruitful discussions and encouragement. This research was supported by JSPS KAKENHI Grants No. JP17J02020 and No. JP20H00140. This work was partially performed on the “Plasma Simulator” (FUJITSU FX100) of NIFS with the support and under the auspices of the NIFS Collaboration Research program (NIFS17KNSS090).

APPENDIX: DEMONSTRATION OF ALMOST-PERFECT REFLECTION VIA DENSITY MODULATION

The wavelength of the ion-acoustic wave excited by the SBS is about half of the whistler wavelength. For the case of Fig. 6(b), the whistler wavelength is the fourth of the injected laser wavelength $\lambda_L/4$, and then the wavelength of the ion-acoustic wave is $\sim \lambda_L/8$. A sufficiently developed ion-acoustic wave generates density modulation, which has a periodic

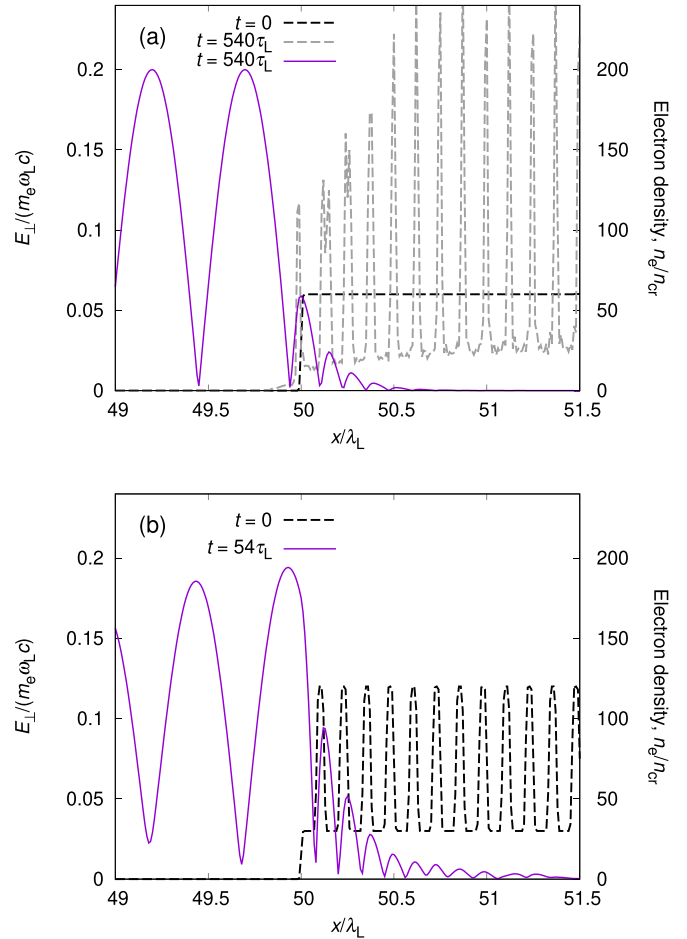


FIG. 9. Perpendicular electric fields of transverse electromagnetic wave and electron density for the same simulation as Fig. 6 (a) and another simulation with density modulation (b), where each color indicates corresponding time and the solid and dashed lines indicate electric fields and electron density, respectively.

structure with the same wavelength as the ion-acoustic wave. Figure 9(a) shows the perpendicular electric fields of electromagnetic wave and electron density at $t = 540\tau_L$ in the same simulation as Fig. 6. There is an apparent periodic structure in the electron density profile, and its period is about $\lambda_L/8$. The initial density is $60n_{cr}$ for this case. However, the lower baseline density becomes around $30n_{cr}$, and the peak density of the bumps reaches over $120n_{cr}$. The optical path difference between reflected waves from adjacent bumps is nearly equivalent to the whistler wavelength. Then it satisfies the condition of the constructive interference for the reflected wave. This mechanism is the same as the principle of the dielectric multilayer mirror. We have simulated the whistler wave propagation to the dense plasma with a significant density modulation to verify this phenomenon.

The baseline and bump densities are set to 30 and $120n_{cr}$, respectively. Assuming the average density is $60n_{cr}$, and the distance between adjacent bumps becomes $\lambda_L/8$, each layer thickness is determined as $d_{bump} = \lambda_L/24$ and $d_{base} = \lambda_L/12$. In this situation, the optical path difference between reflected waves from adjacent bumps is calculated as $2(N_{bump}d_{bump} + N_{base}d_{base}) = 2(\sqrt{3}1\lambda_L/24 +$

$\sqrt{8.5}\lambda_L/12) = \sim 0.95\lambda_L$, which roughly satisfies the condition of the constructive interference, where N_{bump} and N_{base} are the refractive indices for the bump and baseline densities, respectively. Figure 9(b) shows the initial electron density profile and perpendicular electric fields of electro-

magnetic wave at $t = 54\tau_L$. In the simulation, the injected laser interacts with the plasma at $t = 50\tau_L$. Therefore, the laser-generated whistler wave is mostly reflected immediately after laser interacting the plasma for the case with density modulation.

-
- [1] H. Yoneda, T. Namiki, A. Nishida, R. Kodama, Y. Sakawa, Y. Kuramitsu, T. Morita, K. Nishio, and T. Ide, *Phys. Rev. Lett.* **109**, 125004 (2012).
- [2] S. Fujioka, Z. Zhang, K. Ishihara, K. Shigemori, Y. Hironaka, T. Johzaki, A. Sunahara, N. Yamamoto, H. Nakashima, T. Watanabe *et al.*, *Sci. Rep.* **3**, 1170 (2013).
- [3] J. Santos, M. Bailly-Grandvaux, L. Giuffrida, P. Forestier-Colleoni, S. Fujioka, Z. Zhang, P. Korneev, R. Bouillaud, S. Dorard, D. Batani *et al.*, *New J. Phys.* **17**, 083051 (2015).
- [4] K. F. F. Law, Y. Abe, A. Morace, Y. Arikawa, S. Sakata, S. Lee, K. Matsuo, H. Morita, Y. Ochiai, C. Liu *et al.*, *Phys. Rev. E* **102**, 033202 (2020).
- [5] T. Johzaki, T. Taguchi, Y. Sentoku, A. Sunahara, H. Nagatomo, H. Sakagami, K. Mima, S. Fujioka, and H. Shiraga, *Nucl. Fusion* **55**, 053022 (2015).
- [6] S. Sakata, S. Lee, H. Morita, T. Johzaki, H. Sawada, Y. Iwasa, K. Matsuo, K. F. F. Law, A. Yao, M. Hata *et al.*, *Nat. Commun.* **9**, 3937 (2018).
- [7] K. Matsuo, N. Higashi, N. Iwata, S. Sakata, S. Lee, T. Johzaki, H. Sawada, Y. Iwasa, K. F. F. Law, H. Morita *et al.*, *Phys. Rev. Lett.* **124**, 035001 (2020).
- [8] F. F. Chen, *Introduction to Plasma Physics and Controlled Fusion*, Vol. 1 (Springer, New York, 1984).
- [9] D. Strickland and G. Mourou, *Opt. Commun.* **56**, 219 (1985).
- [10] N. Miyanaga, H. Azechi, K. Tanaka, T. Kanabe, T. Jitsuno, J. Kawanaka, Y. Fujimoto, R. Kodama, H. Shiraga, K. Knodo *et al.*, *J. Phys. IV France* **133**, 81 (2006).
- [11] D. Maywar, J. Kelly, L. Waxer, S. Morse, I. Begishev, J. Bromage, C. Dorrer, J. Edwards, L. Folsbee, M. Guardalben *et al.*, *J. Phys. Conf. Ser.* **112**, 032007 (2008).
- [12] J. Crane, G. Tietbohl, P. Arnold, E. Bliss, C. Boley, G. Britten, G. Brunton, W. Clark, J. Dawson, S. Fochs *et al.*, *J. Phys.: Conf. Ser.* **244**, 032003 (2010).
- [13] D. Batani, M. Koenig, J. Miquel, J. Ducret, E. d'Humieres, S. Hulin, J. Caron, J. Feugeas, P. Nicolai, V. Tikhonchuk *et al.*, *Phys. Scr.* **2014**, 014016 (2014).
- [14] I. Pogorelsky, M. Babzien, I. Ben-Zvi, M. Polyanskiy, J. Skaritka, O. Tresca, N. Dover, Z. Najmudin, W. Lu, N. Cook *et al.*, *Plasma Phys. Controlled Fusion* **58**, 034003 (2016).
- [15] J.-J. Berthelier, M. Malingre, R. Pfaff, E. Seran, R. Pottelette, J. Jasperse, J.-P. Lebreton, and M. Parrot, *Nat. Geosci.* **1**, 101 (2008).
- [16] B. Eliasson and K. Papadopoulos, *J. Geophys. Res.* **113**, A09315 (2008).
- [17] X. Shao, B. Eliasson, A. Sharma, G. Milikh, and K. Papadopoulos, *J. Geophys. Res.: Space Phys.* **117**, (2012).
- [18] F. Bagenal, *Annu. Rev. Earth Planet Sci.* **20**, 289 (1992).
- [19] Q. Jia, K. Mima, H.-b. Cai, T. Taguchi, H. Nagatomo, and X. T. He, *Phys. Rev. E* **91**, 023107 (2015).
- [20] M. Hata, H. Sakagami, and A. Das, *J. Phys. Conf. Ser.* **688**, 012027 (2016).
- [21] M. Bailly-Grandvaux, J. Santos, C. Bellei, P. Forestier-Colleoni, S. Fujioka, L. Giuffrida, J. Honrubia, D. Batani, R. Bouillaud, M. Chevrot *et al.*, *Nat. Commun.* **9**, 102 (2018).
- [22] T. Sano, Y. Tanaka, N. Iwata, M. Hata, K. Mima, M. Murakami, and Y. Sentoku, *Phys. Rev. E* **96**, 043209 (2017).
- [23] S. X. Luan, W. Yu, F. Y. Li, D. Wu, Z. M. Sheng, M. Y. Yu, and J. Zhang, *Phys. Rev. E* **94**, 053207 (2016).
- [24] X. Yang, W. Yu, H. Xu, M. Yu, Z. Ge, B. Xu, H. Zhuo, Y. Ma, F. Shao, and M. Borghesi, *Appl. Phys. Lett.* **106**, 224103 (2015).
- [25] T. Sano, M. Hata, D. Kawahito, K. Mima, and Y. Sentoku, *Phys. Rev. E* **100**, 053205 (2019).
- [26] T. Sano, S. Fujioka, Y. Mori, K. Mima, and Y. Sentoku, *Phys. Rev. E* **101**, 013206 (2020).
- [27] Y. Tong, I. Y. Vasko, M. Pulupa, F. S. Mozer, S. D. Bale, A. V. Artemyev, and V. Krasnoselskikh, *Astrophys. J. Lett.* **870**, L6 (2019).
- [28] Y. Tong, I. Y. Vasko, A. V. Artemyev, S. D. Bale, and F. S. Mozer, *Astrophys. J.* **878**, 41 (2019).
- [29] K. Nishikawa, *J. Phys. Soc. Jpn.* **24**, 916 (1968).
- [30] D. Forslund, J. Kindel, and E. Lindman, *Phys. Rev. Lett.* **29**, 249 (1972).
- [31] K. F. Lee, *Phys. Fluids* **17**, 1343 (1974).
- [32] Y. Ke, X. Gao, Q. Lu, and S. Wang, *Phys. Plasmas* **24**, 012108 (2017).
- [33] Y. Sentoku and A. J. Kemp, *J. Comput. Phys.* **227**, 6846 (2008).